

## ORGANISMAL BIOLOGY

## Electrical signaling and coordinated behavior in the closest relative of animals

Jeffrey Colgren and Pawel Burkhardt\*

The transition from simple to complex multicellularity involves division of labor and specialization of cell types. In animals, complex sensory-motor systems are primarily built around specialized cells of muscles and neurons, though the evolutionary origins of these and their integration remain unclear. Here, to investigate sensory-behavior coupling in the closest relatives of animals, we established a line of the choanoflagellate, *Salpingoeca rosetta*, which stably expresses the calcium indicator RGECO1. Using this, we identify a previously unknown cellular behavior associated with electrical signaling, in which ciliary arrest is coupled with apical-basal contraction of the cell. This behavior and the associated calcium transients are synchronized in the multicellular state and result in coordinated ciliary arrest and colony-wide contraction, suggesting that information is spread among the cells. Our work reveals fundamental insights into how choanoflagellates sense and respond to their environment and enhances our understanding of the integration of cellular and organism-wide behavior in the closest protistan relatives of animals.

## INTRODUCTION

Animals move through and interact with their environments in ways unique to life on earth. Calcium signaling is at the crux of this sensory-behavioral integration, playing a role in every modality from initial signal detection to downstream responses. This is achieved through dynamic control of free cytoplasmic calcium concentrations, and modulation of entry, release, and clearance. Although the emergence of calcium as a signaling molecule is very ancient, there are marked differences in the mechanisms used by plants, fungi, and animals; the major lineages where complex multicellularity is present (1). It is hypothesized that stable multicellularity provides strong pressure for the development of versatile communication systems between cells. In animals, sensory-motor integration and coordinated behavior is primarily achieved by the activity of specialized cell types, neurons, and myocytes (2–4). These are excitable cells that depend on large and tightly regulated calcium events to trigger a rapid response. On short timescales, this response can act to convert environmental information into electrical or chemical signals, propagate these signals, or convert the signal into force generation or movements. On the basis of their broad phylogenetic distribution, muscles and neurons likely arose very early in animal evolution and potentially multiple times through convergence (5–10). Furthermore, many of the proteins involved in these pathways are also found outside of animals, with a large collection found in the closest unicellular relatives of animals (11–13). However, the function of these components and their level of integration within these organisms largely remains unstudied.

The ability to precipitate phosphate ions makes high calcium concentrations inherently toxic to life as we know it, resulting in strong evolutionary pressure on sequestering, compartmentalizing, and extruding calcium ions (14–16). In animal cells, cytoplasmic levels of free calcium are in the nanomolar range, while extracellular concentrations are in the millimolar range, and major intercellular stores in the micromolar range (up to the millimolar range in excitable cells, such as muscles and neurons) (14–16). Calcium is an important secondary messenger in animal excitable cells. As a general

mechanism, membrane depolarization activates voltage-gated calcium channels (VGCCs), which leads to an influx in calcium. This influx can then trigger an immediate response (such as vesicle fusion in neurons) or further release of calcium stores (as in muscle contraction). These are transient events, and clearing of signal occurs via segregation by calcium binding proteins, compartmentalization into internal stores, and/or extrusion from the cell (17–19).

VGCCs are broadly distributed in eukaryotes and have been shown to influence/regulate flagellar movements in paramecium and *Chlamydomonas* (20, 21) and mediate infection by various parasitic protists (22), as well as leaf movement in plants (23). In animals, these channels can be broadly characterized into low-voltage activation and high-voltage activated channels (24). Phylogenetic analyses have shown that choanoflagellates, the closest known living relative to animals, have a single member of each of these categories (25).

Choanoflagellates are bacterivorous filter feeders and are highly polarized cells characterized by a single apical flagellum, surrounded by a microvilli-based collar (Fig. 1A). The planar beating of the flagellum generates flow, which draws bacterial prey into contact with the collar where it is phagocytized (Fig. 1B). Choanoflagellates have complex life cycles, with some displaying transient multicellularity, which is generally achieved through serial cell division (26). The choanoflagellate model *Salpingoeca rosetta* has at least six distinct cell stages: linear chain colonies, rosette colonies, slow swimming solitary cells, fast swimming solitary cells, attached cells, and ameboid-like cells following physical confinement (27, 28). Both chain colonies and rosette colonies occur through serial cell division followed by incomplete abscission, which leaves a small cytoplasmic bridge between the cells (27, 29) (Fig. 1C). These bridges have only been observed by electron microscopy and contain two electron-dense structures each localized near one of the cells. Under nutrient-rich conditions, cells divide rapidly in chains before separating into slow swimmers. Environmental cues, such as the presence of specific bacterial sulfonolipids, can trigger the development of rosette colonies (30). In this case, the cells secrete extracellular matrix (ECM) from their base into the central region of the group of cells. The result is a multicellular ball with the collars and flagella facing outward. The cytoplasmic bridges are maintained in this state and can take on a highly complex arrangement (29).

Michael Sars Centre, University of Bergen, 5008 Bergen, Norway.

\*Corresponding author. Email: pawel.burkhardt@uib.no

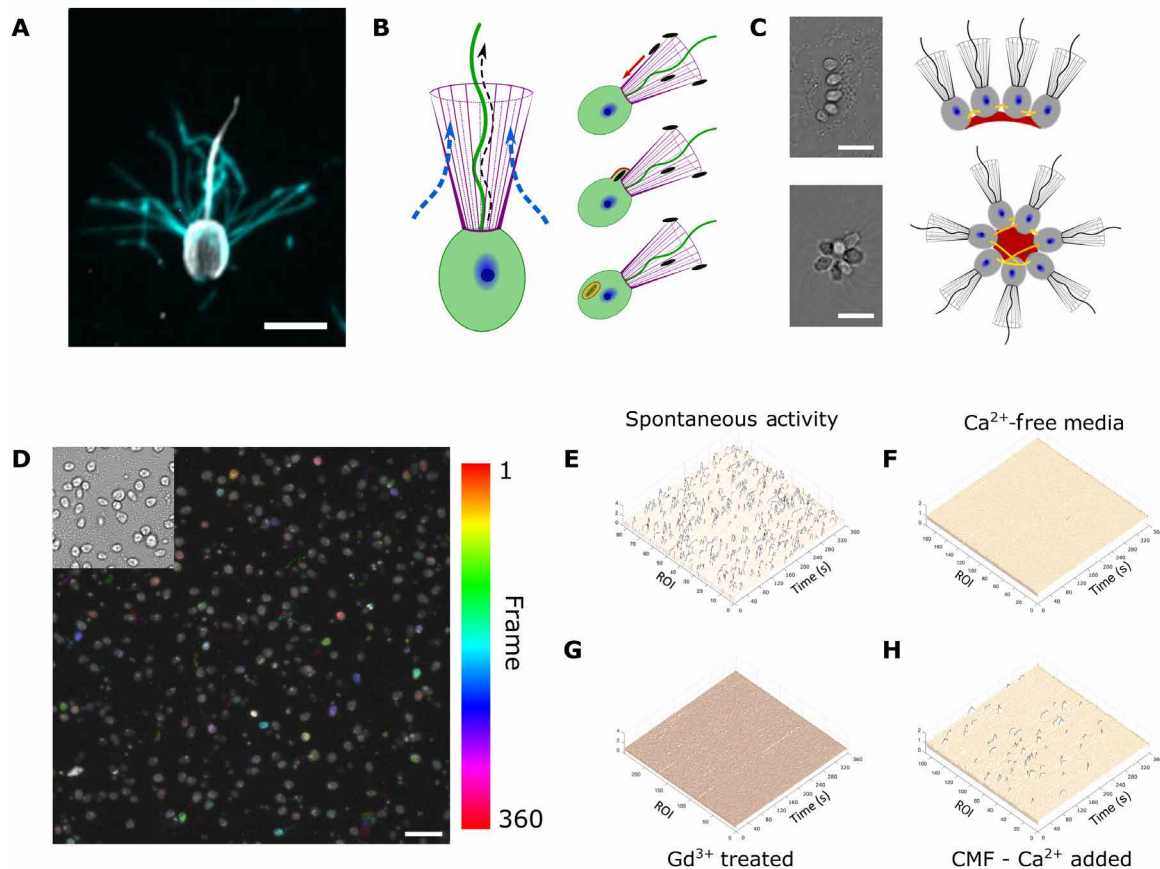


**Fig. 1. Choanoflagellate morphology, feeding, and spontaneous  $\text{Ca}^{2+}$  dynamics.** (A) Unicellular state of *Salpingoeca rosetta*, showing tubulin (gray) and actin filaments (cyan), the polarized cell has a single flagellum (cilia) surrounded by a microvilli-based collar. (B) Planar beating of the flagellum draws water through the microvilli collar where bacterial prey can become trapped. Prey is phagocytized at the base of the collar. (C) Multicellular states in *S. rosetta* form through serial division, resulting in chains (top) or rosettes (bottom). Cells are connected by thin intercellular bridges (yellow/orange in diagrams) and share ECM (red). In rosette, filopodia (gray) at the base of the cells extend into a thick ECM orienting the collar and flagella outward. Intercellular bridges do not have a stereotyped pattern in colonies. (D) Time series projection of RGECO signal in cells over 360 s of a spontaneously acting culture. Upper left shows a still of simultaneously acquired DIC images of the culture. (E)  $\Delta F/F_0$  (z axis) traces for all cells (y axis) over time (x axis) in a spontaneously acting culture. (F) A mirror culture plated in calcium-free media shows complete loss of spontaneous activity. (G) A mirror culture treated with  $\text{Gd}^{3+}$  also shows complete loss of spontaneous activity. (H) Series from the CFM culture, following introduction of 10 mM  $\text{Ca}^{2+}$  shows a return of spontaneous activity. Scale bars, 5  $\mu\text{m}$  (A) and 20  $\mu\text{m}$  [(C) and (D)]. s, seconds.

Although morphologically simple compared to animals, choanoflagellates have been extremely successful, being found throughout the world's oceans. There is evidence that the general morphology has existed for at least 600 million years, and it has been hypothesized that the first animal resembles a choanoflagellate colony (26, 31, 32). Choanoflagellates have also been shown to demonstrate behaviors such as chemotaxis, aerotaxis, and pH-taxis (33, 34), and have a large toolkit of ion channels and calcium-binding proteins that function in animal sensory motor circuits (1, 11, 12, 15, 25).

Here, we report on the calcium dynamics in the choanoflagellate *S. rosetta*, in both unicellular and multicellular stages. We find a range of spontaneous  $\text{Ca}^{2+}$  transients, which can be grouped into discrete categories. We identify categories associated with VGCC activity and use this “calcium signaling vocabulary” to identify a previously unknown cell behavior. Furthermore, we find evidence of regulated flow of signal between the cells in colonies. We find that chains, the more transient form of multicellularity, show predominantly asynchronous events between cells, while the more stable rosette colonies demonstrate predominantly synchronous events.

### Spontaneous calcium transients in single cells

To probe  $\text{Ca}^{2+}$  dynamics in *S. rosetta*, we established a line stably expressing the  $\text{Ca}^{2+}$  indicator RGECO (see Materials and Methods and the Supplementary Materials for a detailed workflow). Imaging of a culture in the unicellular stage revealed a large amount of spontaneous activity (Fig. 1, D and E; fig. S1; and movie S1). This activity could be completely ablated by removal of extracellular calcium from the culture media (Fig. 1F and fig. S2). The same results could be obtained by incubating cells in media containing the nonspecific  $\text{Ca}^{2+}$  channel inhibitor gadolinium (5  $\mu\text{M}$   $\text{Gd}^{3+}$ ) (Fig. 1G and movie S1). Addition of external  $\text{Ca}^{2+}$  back to the calcium-free media (CFM) showed a return of activity (Fig. 1H). Together, this suggests that the spontaneous activity is dependent on  $\text{Ca}^{2+}$  entry from the extracellular environment.

Next, to understand whether there is any synchronicity within the spontaneous activity, we performed network analysis on active cultures. The large number of transients showed a range of amplitudes as well as rise and fall times, with rising slightly faster than fall time (fig. S3). Analysis of pairwise synchronization identified seven

clusters of activity (fig. S3), while functional connectivity analysis did not identify major nodes of activity (fig. S3). Looking at the physical locations of individual cells within clusters suggests that the majority of synchronous activity is the result of random chance. However, clusters show some arrangement in space, suggesting that activity may be tied to local environmental conditions (fig. S3).

Our choanoflagellate cultures are grown with *Echinicola pacifica* feeder bacteria as the sole food source. We hypothesized that grouping of bacteria may be a determinant of the localized activity. To test this, cultures were extensively washed with artificial seawater (ASW) to remove as much bacteria as possible. This culture was then split and plated without bacteria or with bacteria added back. In minimal bacteria cultures, spontaneous activity occurred at a rate of 0.027 events per minute per cell, while cultures provided a large amount of bacteria showed activity at a rate of 0.356 events per minute per cell (Fig. 2A, fig. S4, and movie S2). This suggests that at least some of the activity is dependent on the sensation of bacteria or feeding behavior.

To better understand activity of these cells, we perfused them with depolarizing concentrations of  $K^+$  (25 mM) while imaging and observed a highly synchronized response across the field of view (Fig. 2B and movie S1). This could also be achieved with the treatment of 10  $\mu$ M adenosine triphosphate (ATP) (fig. S5). To validate that this response arises from cellular depolarization, we fabricated a culture dish to allow for electric field stimulation (see Materials and Methods) and applied sequential 10-V pulses or a single 50-V pulse (Fig. 2B and fig. S5). This resulted in a synchronized calcium

transient across the culture followed by a return to asynchronous activity. All cases of stimulation elicited transient events, while treatment with the calcium ionophore, ionomycin (1  $\mu$ M), showed a stable increase with limited bleaching of using the same acquisition settings (fig. S6). Because depolarization could elicit a consistent response, we used the VGCC inhibitor verapamil for treatment and found that it reduced, but did not completely ablate, spontaneous activity (Fig. 2B and movie S1). Together, this suggests that consistent transients can be induced by activating voltage-gated channels and that at least some of the transients observed in spontaneously acting cultures are dependent on VGCC activity.

### VGCC-dependent transients

The *S. rosetta* genome contains two putative VGCCs (SrCa<sub>v</sub>1/2; PTSG\_09464 and SrCa<sub>v</sub>3; PTSG\_03773). To understand the contribution of VGCC in the spontaneous activity of cultures, we treated them with increasing concentrations of the VGCC inhibitor verapamil and found a dose-dependent decrease in spontaneous activity (Fig. 2B, fig. S7, and movie S1). However, spontaneous activity was still present until lethal concentrations of verapamil were applied (fig. S7). This inability to mirror the complete loss of activity as with  $Gd^{3+}$  treatment suggests that some of the spontaneous activity relies on entry through verapamil-insensitive channels. To extract information encoded in individual  $Ca^{2+}$  transients, we applied kShape clustering as a nonbiased means of grouping events. We clustered individual events within spontaneous acting cultures,  $K^+$ -stimulated cultures, and verapamil-treated cultures and identified six major

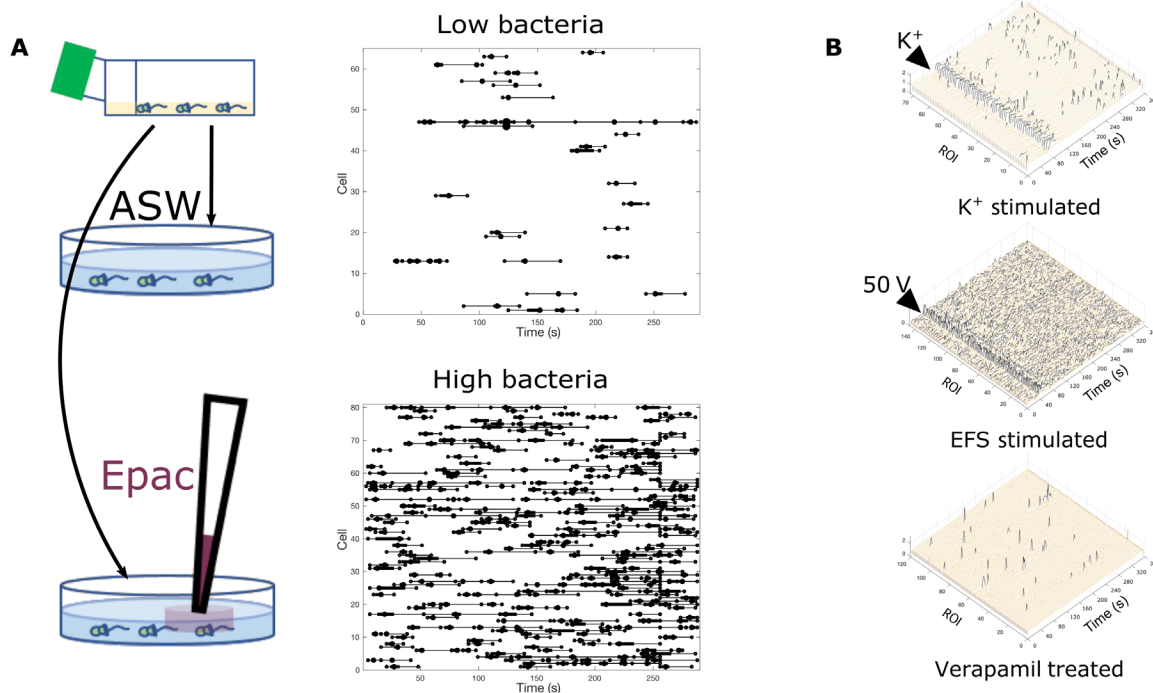


**Fig. 2. Spontaneous activity increases with prey abundance and transients can be controlled by voltage-gated calcium channel activity.** (A) Cultures were thoroughly washed with artificial seawater (ASW) and then plated in ASW or ASW with a known quantity of feeder bacteria. Raster plots for washed culture (top) and mirror culture with bacteria reintroduced (bottom), where regions of interest (ROIs) correspond to cells (y axis) over time (x axis) with dots indicating peaks and whiskers indicating rise and fall. (B) Perfusion of 25 mM  $K^+$  ( $T = 80$  s) triggers a highly synchronized event within the field of view. This can also be achieved with electric field stimulation, by applying a 50-V pulse ( $T = 40$  s). Treatment with the voltage-gated calcium channel inhibitor, verapamil (10  $\mu$ M), greatly decreases spontaneous activity. EFS, electric field stimulation. s, seconds.

classes of peaks (Fig. 3A). By looking at how the proportions of these events changed in relation to different conditions, we identified clusters 4 and 5 as likely being dependent on VGCCs, owing to a decrease following verapamil treatment and an increase following stimulation (Fig. 3B). These clusters also showed an increased proportion in the high bacteria culture (Fig. 3B).

Next, we wanted to see whether the different classes of transients could be correlated with any type of cellular behavior. Looking at differential interference contrast (DIC) images of cells during class 4 and 5 events, we found an obvious change in cell morphology, generally consisting of rounding up from apparent constriction along the apical-basal axis followed by a return to a more polarized shape during dissipation of the  $\text{Ca}^{2+}$  signal (Fig. 3C and movie S3). This “behavior” could be triggered by treatment with depolarizing concentrations of  $\text{K}^+$ , concurrent with the synchronized transient event (Fig. 3C and movie S3). These events can be generally characterized as a significant increase in circularity and decrease in aspect ratio ( $P$  values  $< 0.001$ ) followed by a significant decrease in circularity and increase in aspect ratio ( $P$  values  $< 0.001$ ). The duration of the constriction and relaxation closely mirrored the  $\text{Ca}^{2+}$  transients. During these events, bacteria could also be seen being displaced from the feeding collar (Fig. 3D and movie S3). Quantification of bacterial abundance before and after stimulation revealed a significant decrease in bacteria at the collar. Displacement of bacteria suggested that flow around the collar is altered during the event. Using high-speed imaging, we watched flagellar movement during spontaneous and triggered events and found that the flagellum paused during the events, followed by a brief period of asynchronous beating, before returning to the normal pattern (Fig. 4A and movie S4), which occurs in a synchronized manner following stimulation (Fig. 4B). The initial rise in cytosolic  $\text{Ca}^{2+}$  levels could be detected before flagellar arrest, suggesting that the signal is propagated to the flagellum rather than from it (Fig. 4C, fig. S8, and movie S4). High-speed imaging of the cells undergoing flagellar arrest showed a straightening of the flagellum from the base toward the tip (fig. S9 and movie S4). For individual cells, the stereotyped sequence involved a cytoplasmic rise in  $\text{Ca}^{2+}$  followed closely (30 to 60 ms) by flagellar arrest, which was followed by apical-basal contraction during the peak of  $(\text{Ca}^{2+})_{\text{cyto}}$ . As RGECCO signal returned to baseline, flagellar beating resumed before the return of cell shape (Fig. 4D).

### Activity in colonies

*S. rosetta* has at least five distinct cell stages including multicellular colonies consisting of either rosettes or linear chains (27). These multicellular stages are inducible by environmental factors and form through serial cell division. To understand multicellular  $\text{Ca}^{2+}$  dynamics, we induced colony formation in our RGECCO expressing line. In both rosettes and chain colonies, we found that spontaneous activity occurred in a synchronized manner across the colony (Fig. 5A and movie S5). As in single cells, spontaneous events remained dependent on external  $\text{Ca}^{2+}$  availability and transients could be induced by depolarization. In chain colonies, the rapid depolarization of the full colony often led to separation of the cells. In spontaneously acting cultures, synchronized and asynchronous transients, across the colonies, were observed in both rosette and chain colonies (Fig. 5B). The frequency of occurrence of each differed substantially between the two stages. In rosette colonies, synchronized transients were most frequent, making up 62.93% of the events. Nonmaximal synchronized events (characterized as at least one cell, but not every cell) occurred at

33.6%. However, in 3.45% of active rosettes, colonies showed rapid (within 3 s) asynchronous transients between the component cells (Fig. 5A and movie S5). These showed no pattern within spread around the colony. (Fig. 5A and movie S5). On the other hand, asynchronous events seemed to dominate the spontaneous activity in chains, comprising 77.88% of observed events. Synchronization within a subset of the colony was observed 8.85% of the time, while synchronous transients across the colony was observed 13.27% of the time (Fig. 5, A and B, and movie S5).

Strong transient events associated with the behavior described in single cells were observed in colonies and depolarization of the cells triggered a similar response. In rosette colonies, this led to a contraction of the full colony (Fig. 5C and movie S6). In addition, similar to the single cells, the flagellar beating would briefly arrest (Fig. 5D, fig. S10, and movie S6) during the event and bacterial shedding could be observed (fig. S11). Furthermore, as with solitary cells, increasing the concentration of bacteria in the culture increased the frequency at which spontaneous transients occurred (fig. S12). When these events occurred, they were synchronized across the colony. Cytoplasmic  $\text{Ca}^{2+}$  levels began to rise before flagellar arrest, with similar kinetics, and spread of signal could be observed between the cells within the focal plane for which flagella were also visible (Fig. 5D and movie S6). Transients in rosettes, which were associated with the behavior described in single cells, showed similar dynamics, where flagellar arrest initiated shortly after the rise in cytoplasmic calcium levels and both are followed by apical basal contraction (Fig. 5E). Subtle spread of calcium signal could be detected between cells, as could disparity in flagellar arrest.

### DISCUSSION

One of the fundamental questions of the origins of complex multicellularity is how isolated cells coalesce into larger assemblages capable of specialization and coordinated behavior. Our observation of both synchronized and asynchronous transients in colonies suggest that regulated signaling occurs between these cells. Cells in colonies are linked by thin cytoplasmic bridges, believed to result from incomplete abscission (27, 29). The molecular composition of the cytoplasmic bridges between cells remains elusive. However, the tight synchronization observed in rosettes suggests that these connections are at least permeable to ions. The observed asynchronous activity within colonies further suggests that there is no open flow of ions between cells, but rather a regulated process. The notable disparity in frequency of synchronized events in rosette colonies and chain colonies suggests that there is a fundamental difference in these two multicellular states. Chain colonies are transient and undergo abscission at bridges, so it is likely that the observed increase in asynchronous activity is a result of the loss of this channel of communication. However, it could also be a result of different geometries of the colonies. Cells in rosettes extend basal filipodia into the ECM core that are in close proximity to each other (27, 29), which are absent in chains. These could serve as signaling hubs, independent of the cytoplasmic bridges. Future studies will be needed to elucidate this.

Increased synchronization is consistent with communication and coordination across colony, which allows it to act more as an individual unit as opposed to a collective. It is hypothesized that rosette colony formation primarily acts as a means of increasing feeding efficiency in food-rich environments or as a means of increasing size



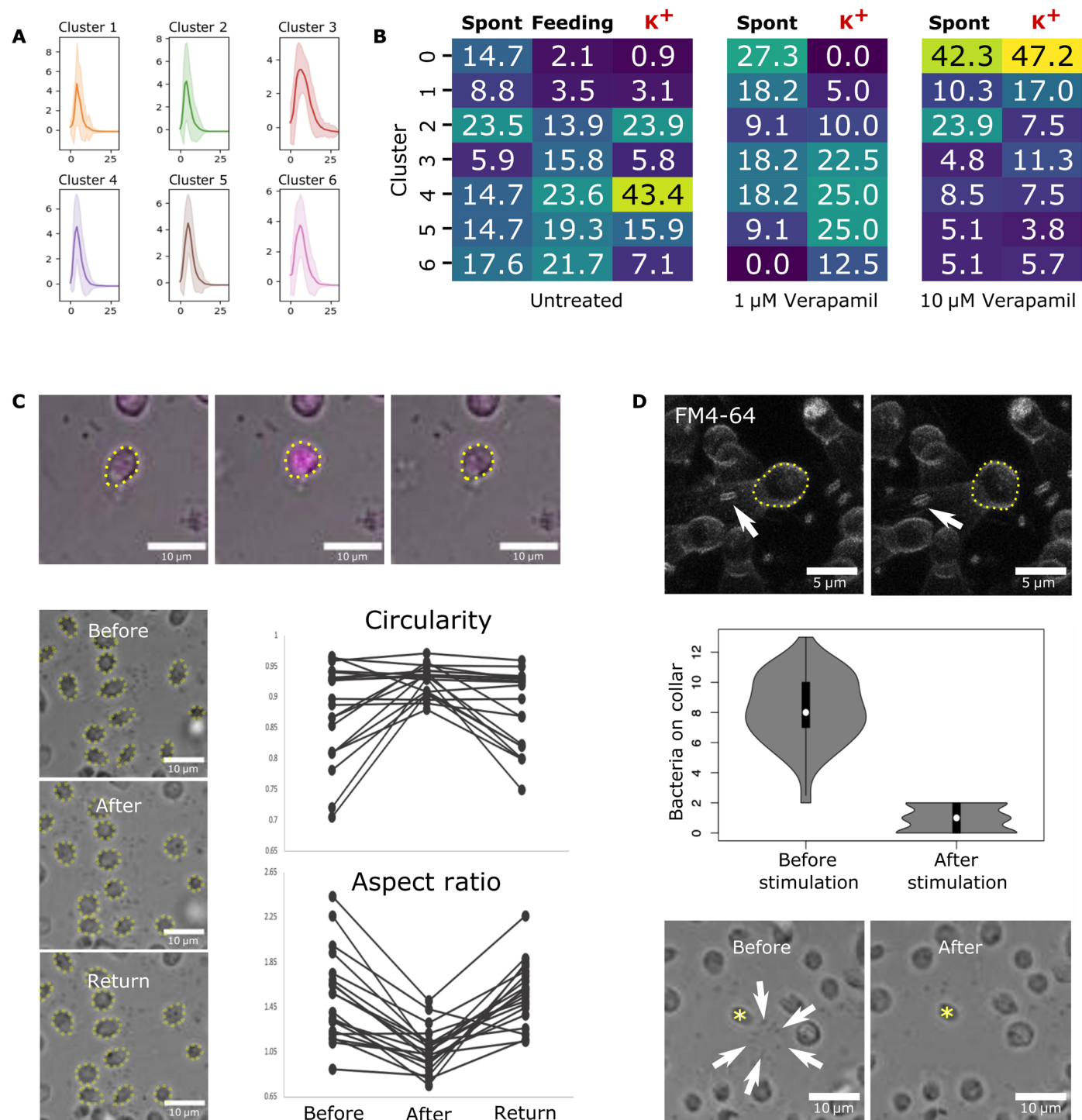


**Fig. 3. Events associated with VGCC activity are associated with a cellular behavior.** (A) K-shape peak clusters from aligning individual peaks from spontaneously activity in normal culture, high bacterial, and verapamil treated, as well as from K<sup>+</sup> stimulated. (B) Heatmap showing proportion of peaks that fall into each cluster in the different treatment conditions. Clusters 4 and 5 show the largest positive change to stimulation and negative change following verapamil treatment. (C) Top shows a DIC image overlaid with RGECO signal (magenta) of a cell undergoing a spontaneous event. The cell is outlined with yellow showing a shape change during the event. Bottom shows several cells in a field of view undergoing a synchronized shape change following stimulation with K<sup>+</sup>. Quantification of circularity and aspect ratio of each cell shows a rounding up followed by return to original polarized shape during the event. (D) FM4-64-labeled cell (yellow outline) and bacterium (white arrow) at the collar shows displacement of the bacteria during the shape change event. Below, quantification of visible bacteria on the cell's collars before and just after stimulation. Still images show bacteria (white arrows) visible on the collar of a cell (yellow asterisk) before and after stimulation.

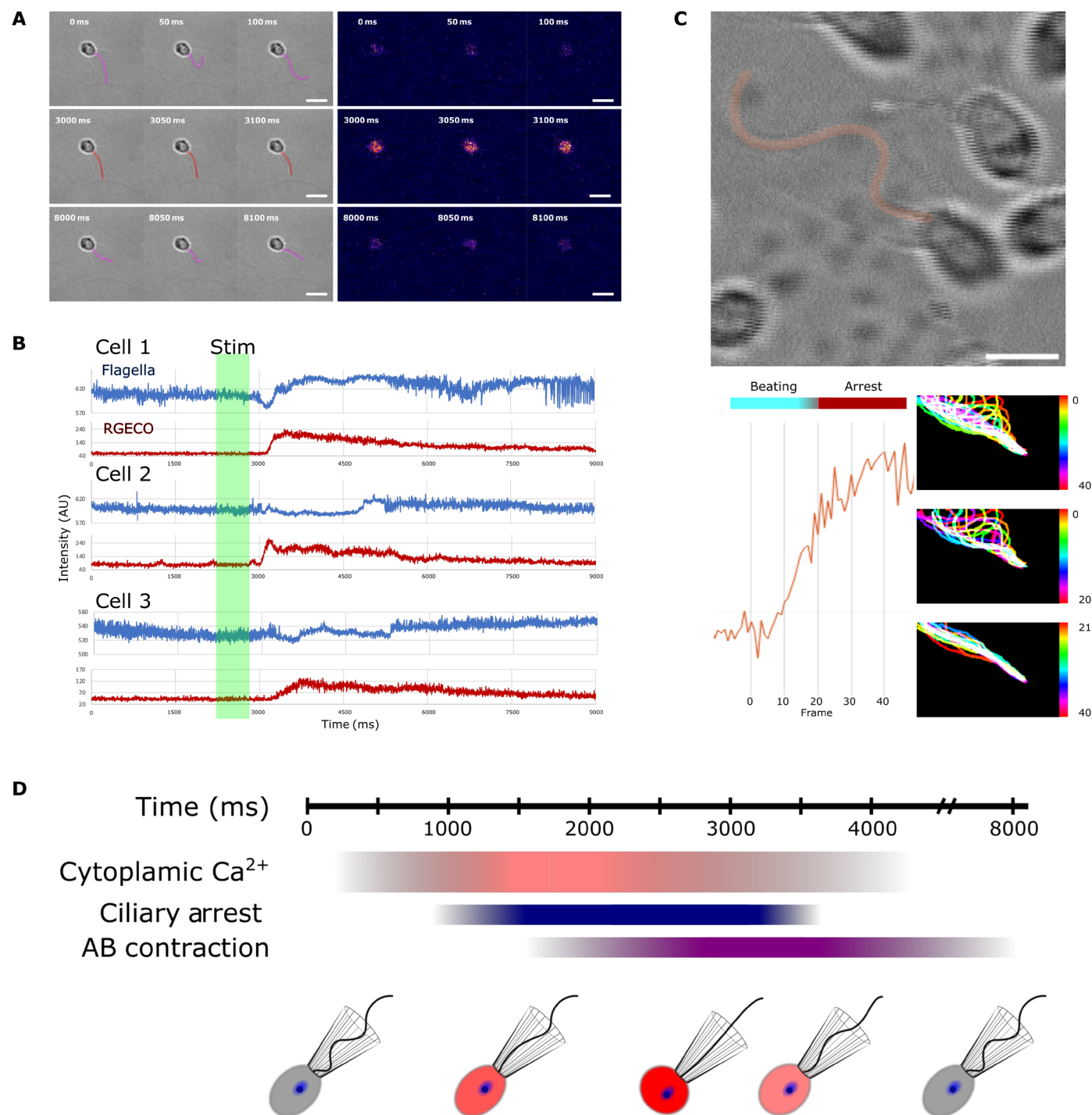


**Fig. 4. Calcium regulates flagellar arrest.** (A) Flagellar beating arrests during events. Rows show three frames of overlapping DIC and RGECO images with the flagella highlighted in magenta (top and bottom) or red (middle). Series occur before (top), during (middle), and after (bottom) the event. (B) The blue line shows pixel intensity of line scan taken parallel to the flagella originated from the base in the DIC images. Consistent beating shows periodic maximum and minimum values as the flagella passes the line, while changes in beating alter this pattern. The red line shows intensity of RGECO signal in the cell body. The green bar indicates when  $\text{K}^+$  was perfused into the culture. (C) Dual recording of RGECO signal and flagellar beating shows that arrest occurs after the initial increase in calcium concentration in the cell body. Bottom shows RGECO trace in ~30-ms frames on the left, with temporal projections of the flagella on the right. Top shows the projection over 40 frames during which RGECO signal reaches its maxima, the middle shows the first 20 frames, and the bottom shows the last 20 frames. (D) General sequence of events for behavior. Initial rise in cytoplasmic RGECO signal peaks in ~1000 ms and plateaus for ~400 ms before returning to baseline levels over ~2500 ms. Ciliary arrest begins 600 to 900 ms and takes ~600 ms to fully arrest. Beating returns with the drop in cytoplasmic calcium levels. Apical-basal (AB) contraction begins about 500 ms after the onset of ciliary arrest and continues for around 2000 to 3000 ms before gradually returning to the initial shape. Scale bars, 5  $\mu\text{m}$  [(A) and (C)]. ms, milliseconds.

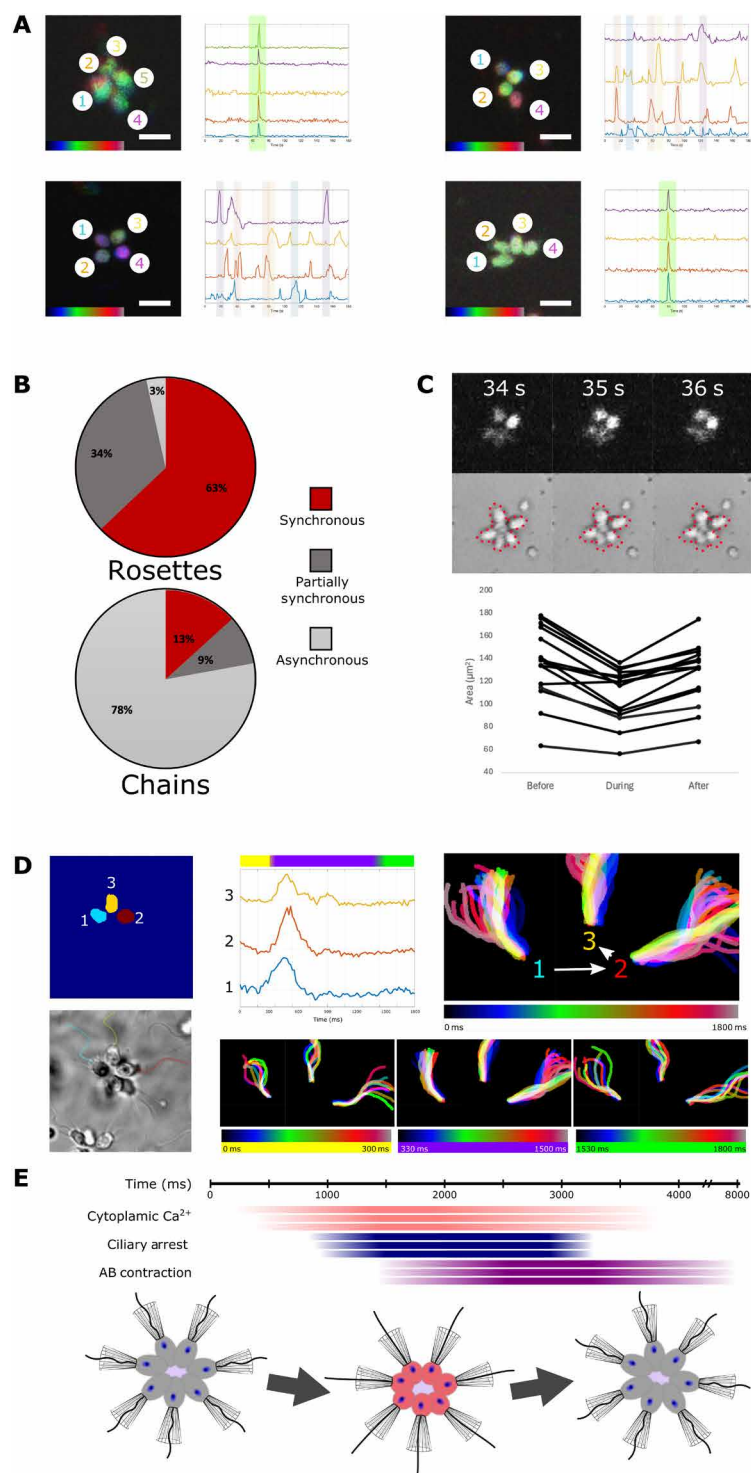


**Fig. 5. Both synchronized and asynchronous events occur in colonies and the described behavior is synchronized.** (A) Rosette colonies primarily show highly synchronized (top) but do have asynchronous events (bottom). Chains primarily show asynchronous events (top) while synchronous ones are present. Graphs show RGECO intensities for each cell, with color matching the number in the temporal projections. (B) Quantification of the occurrence of synchronized, partially synchronized (two or more cells), and asynchronous (multiple cells at different times) in spontaneously acting cultures. (C) RGECO (top) and DIC (bottom) images during an event show coordination of signal and contraction in the colony. Cross-sectional area of various rosette colonies before, during, and after induced events. (D) High-speed imaging of spontaneous activity in a rosette shows synchronized flagellar arrest as well. RGECO signal first increases in cell 1, before visibly increasing in cells 2 and 3. All three visible flagella stop beating around 60 to 90 ms after signal increase, and show a synchronized arrest. Temporal projections of flagella show the total time series, with the bottom panels showing the first 300 ms during which cytoplasmic calcium increases, the ~1200 ms that beating is arrested, and the recovery period. (E) General sequence of events observed in colonies. The sequence follows what is observed in single cells. The three colored bars represent individual cells of a colony as in (D) showing subtle disparities between initial calcium influx and ciliary arrest timing. Scale bars, 10  $\mu\text{m}$ . s, seconds. ms, milliseconds.

to decrease predation (35–40). While these are not mutually exclusive, and have both been documented in different instances of simple multicellularity, evidence suggests that it does not lower rates of predation in choanoflagellates (36). Although the contraction and flagellar arrest behavior occurs in colonies, it does so at a reduced rate, which is consistent with a higher holding capacity in the multicellular stage compared to the unicellular stage. Although further studies will need to be done, our findings are consistent with rosette formation functioning to optimize feeding efficiency.

In extant glass sponges, animals lacking both muscles and neurons, feeding is performed by drawing water through their body, via the beating of flagella in choanocytes, while food particles are trapped and phagocytized at the microvilli collar. These animals are composed of syncytial tissue that propagates action potentials, resulting in the coordinated and transient arrest of flagellar beating (41). This coordinated behavior is thought to regulate the flow rate through their aquiferous system to maximize feeding efficiency (41–43). Although the notable similarity to what we have found in choanoflagellate colonies could have arisen by convergent means, if this dates back to the last common ancestor of choanoflagellates and sponges, then it likely played an important role in animal multicellularity. Our findings suggest an important role of electrical signaling feeding behavior for *S. rosetta*. Although we find instances of phagocytic cups forming during strong calcium transients (fig. S13), the primary response appears to consist of the arrest of the flagella, contraction along the apical-basal axis, and shedding of bacteria from the feeding collar. Modeling of choanoflagellate filter feeding suggests that the bacterial load on the collar strongly affects the ability of the flagella to generate flow as well as the cells' ability to propel itself forward (44, 45). It is possible that the here described behavior functions to balance feeding efficiency with the ability to disperse or simply maintain a high level of flow through the collar region. In freely moving rosette colonies, we observe synchronized events, with no evidence of directional steering (fig. S14). On the basis of the modeling studies, it is not immediately clear how the shape change in rosettes would affect feeding. However, it is important to note that these are transient events, only lasting up to 8 s. It is possible that the change in density resulting in increased packing of the colony allows a subtle dispersal, when coupled with total flagellar arrest. Choanoflagellates primarily interact with their environment by drawing it toward the cell through flagellar beating (25, 46). Although raised in the laboratory with a single bacterial food source, the environments and microenvironments that these cells live in are not static and can contain bacterial blooms and swings of nutrient availability, as well as predators. This creates strong selective pressure for tight regulation of this process.

The capacity to move through and rapidly respond to a changing environment is a hallmark of animal biology. It has been hypothesized that early animal motility relied on coordinated regulation of ciliary beating across the organism (47, 48) and likely was regulated by  $\text{Ca}^{2+}$  (11). However, much of this likely occurred during the time between the first obligately multicellular animal and the last common ancestor of extant lineages. The ability to directly sense and respond to gradients of stimuli in the environment is fundamentally constrained by a cell's size (49, 50). As microeukaryotes, *S. rosetta* is approaching the lower limit on spatial sensitivity in its unicellular state. In rosettes, the size of the colony is sufficient to spatially resolve gradients, though prior studies have shown no coordination in the flagellar beating (51). Here, we find evidence that information

flows between cells of a choanoflagellate colony in a regulated manner. Action potential-like control of ciliary activity has been reported in a variety of protists, often involved in facilitating and modifying movement (47, 48, 52). We find that the stereotyped response of ciliary arrest coupled with apical-basal contraction of the cell is synchronized with signaling across rosettes, culminating in a coordinated behavior. Information spread and coordination across a colony/mass of cells allows this to act as a single unit, meaning cells sample the environments across the full surface area, without the need to directly contact it. This is an essential step to open evolutionary space for modularization and sub-functionalization of cell states and may have helped provide the platform for complex multicellularity to arise in animals.

## MATERIALS AND METHODS

### *S. rosetta* cell culture and colony induction

*S. rosetta* (American Type Culture Collection: PRA-390) was cultured with a single bacterium *E. pacifica* as described in Booth *et al.* (53). Freezer stocks were thawed and seeded into 0.2× high-nutrient media (HNM) (54) and grown for 3 to 5 days. Cultures were then maintained in HNM at 22°C and 60% relative humidity and were passaged at 1:60 every 2 days. Rosettes were induced by inoculating cultures with *Algoriphagus machipongonensis*.

### Plasmid design

RGECO1 was codon optimized for *S. rosetta* using highly expressed transcripts (54). Codon optimization was performed with OPTIMIZER (54). gBlocks fragments (Integrated DNA Technologies) were ordered with overhangs to facilitate HiFi assembly (New England Biolabs; E2621). The codon-optimized RGECO1 was cloned into the *S. rosetta* expression plasmid NK802 (Addgene; #166056) (28) replacing the mCherry sequence. The assembled plasmid was transformed into NEB 5- $\alpha$  (high efficiency) competent cells (New England Biolabs; C2987). After verifying the sequence, the plasmid was purified using the QIAGEN Endofree plasmid Maxi kit (QIAGEN; 12362). Purified plasmid was concentrated to 5 mg/ml.

### Transfection

Transfection of *S. rosetta* was performed as described in Booth *et al.* (53). Before transfection, cells were seeded at 8000 cells/ml in 40 ml of HNM in a 175-ml culture flask (Sardstedt; 83.3912.502) and grown for 48 hours. On the day of transfection, cells were washed 3× with ASW (400 mM NaCl, 8 mM KCl, 14.8 mM  $\text{MgCl}_2 \cdot 6\text{H}_2\text{O}$ , 20.3 mM  $\text{MgSO}_4 \cdot 7\text{H}_2\text{O}$ , 2.7 mM  $\text{CaCl}_2 \cdot 2\text{H}_2\text{O}$ , 2.38 mM  $\text{NaHCO}_3$ , 10  $\mu\text{M}$  NaBr, 97  $\mu\text{M}$   $\text{H}_3\text{BO}_3$ , 100  $\mu\text{M}$   $\text{SrCl}_2 \cdot 6\text{H}_2\text{O}$ , 10  $\mu\text{M}$  NaF, and 0.2  $\mu\text{M}$  KI) by pelleting at 2000g for 5 min at room temperature (2200g for the last spin). Cells were then resuspended at a concentration of  $5 \times 10^7$  cells/ml and  $5 \times 10^6$  cells were pelleted at 800g for 5 min at room temperature. Supernatant was removed and cells were resuspended in 100  $\mu\text{l}$  of priming buffer [40 mM Hepes-KOH, pH 7.5, 34 mM lithium citrate, 50 mM cysteine, 15% polyethylene glycol, molecular weight 8000 (PEG-8000), and 3  $\mu\text{M}$  papain], and incubated at room temperature for 35 min to digest ECM. Priming was halted by the addition of 10  $\mu\text{l}$  of 10% bovine serum albumin and the cells were pelleted at 1200g for 5 min at room temperature. Primed cells were resuspended in 25  $\mu\text{l}$  of SF-Buffer (Lonza) and placed on ice. The transfection mixture was made of 14  $\mu\text{l}$  of ice-cold SF buffer, 2  $\mu\text{l}$  of SrRGECO plasmid, and 2  $\mu\text{l}$  of carrier plasmid



(pUC19 at 20  $\mu\text{g}/\mu\text{l}$ ). Just before transfection, 2  $\mu\text{l}$  of primed cells was added and the full volume was transferred to a well of a nucleofection cuvette [SF Cell Line 4D X Kit S (32 RCT), Lonza]. A CM-156 pulse was applied in the 4D-Nucleofector (Lonza). One hundred microliters of ice-cold recovery buffer (10 mM Hepes-KOH, pH 7.5, 0.9 M sorbitol, and 8% PEG-8000) was immediately added to the well and gently mixed by tapping on the side. After 5 min, the full contents of the well were transferred to 2 ml of low-nutrient media in a six-well plate and incubated at 22°C and 60% relative humidity for 30 min for cells to recover. Ten microliters of *E. pacifica* (10 mg/ml) was then added to the well and gently mixed. Transfected cells were then incubated at 22°C and 60% humidity.

### Selection for stable integration

Following transfection, cells were incubated for 24 hours at 22°C and 60% humidity. After 24 hours, selection began by the addition of puromycin to a final concentration of 40  $\mu\text{g}/\text{ml}$  and cells were incubated 72 hours at 22°C and 60% humidity and monitored for growth. The upper 1 ml of cells, which contained swimming chain colonies, was removed and pelleted at 2000g for 10 min at room temperature. The cells were then resuspended in 2 ml of HNM containing puromycin (80  $\mu\text{g}/\text{ml}$ ) and incubated at 22°C and 60% humidity for 48 hours. After incubation, washing was performed again but cells were resuspended in 12 ml of HNM + 80  $\mu\text{g}/\text{ml}$  and plated across a six-well plate (Thermo Fisher Scientific; 140685). Cells were then incubated for 72 hours at 22°C and 60% humidity. Wells were monitored for growth and washing steps were repeated two times for actively growing cultures. Once consistent growth was observed, cultures were passed 1:10 into fresh selection media and incubated for 48 hours at 22°C and 60% humidity. This was repeated two times. Small aliquots of each culture were then taken and the presence of fluorescence was confirmed by addition of ionomycin (100  $\mu\text{g}/\text{ml}$ ; Millipore; 407950). Cultures that showed RGE01 signal were then diluted to 3 cells/ml in selection media and plated in 100- $\mu\text{l}$  volumes on 96-well plates. Plates were then incubated for 96 hours at 22°C and 60% humidity and monitored for growth. Wells showing growth were marked and passed 1:10 into fresh selection media in 96-well plates. This was repeated two times, after which 58 actively growing monoclonal cultures had been isolated. These cultures were screened for fluorescence signal by mixing 1  $\mu\text{l}$  of culture with 1  $\mu\text{l}$  of ionomycin solution (100  $\mu\text{g}/\text{ml}$  final concentration) and viewing through a red fluorescent protein (RFP) filter. 26 of these cultures, which showed a strong even signal, were then passed (1:10) into 300  $\mu\text{l}$  of selection media in a 48-well plate and incubated for 48 hours at 22°C and 60% humidity. After growing to density, 100  $\mu\text{l}$  of each of these cultures was screened live and during perfusion of ionomycin (100  $\mu\text{g}/\text{ml}$  final concentration) to judge the dynamic range of the sensor. Cultures that showed low baseline signal but strong maximal signal were then scaled up and frozen in 1:10 dimethyl sulfoxide (DMSO) overnight in a Mr. Frosty freezing container (Thermo Fisher Scientific—5100-0001) at  $-80^{\circ}\text{C}$  and then stored in liquid nitrogen. To establish running cultures, vials were thawed at room temperature and then added (1:10) to low-nutrient media containing puromycin (40  $\mu\text{g}/\text{ml}$ ). Growth was monitored alongside wild-type cultures that were not under selection (fig. S15).

### Plating and imaging

General imaging was performed on running cultures at a density of  $\sim 10^6$  cells/ml that were between passages 4 and 15. Glass-bottom

dishes (MatTek—P35G-1.5-10-C) were prepared by adding a drop of poly-L-lysine solution (0.01%) (Sigma-Aldrich—A-005-C) and incubating at room temperature for 30 min. Following incubation, the glass was washed 3X with ASW. Meanwhile, 1 ml of cell culture was washed of excess bacteria by pelleting at 1500g for 10 min at 4°C and the supernatant was carefully removed (using a gel loading tip for the final amount). Cells were then washed and re-pelleted in 1 ml of ASW. The washed pellet was then resuspended in 100  $\mu\text{l}$  of ASW and transferred to the microwell of the glass-bottom dish and incubated for 30 min at room temperature. Following incubation, an additional 100  $\mu\text{l}$  of ASW was gently pipetted into the microwell to overfill it and the rest of the dish was filled with 2 ml of ASW without disturbing the well and cells were imaged.

### Imaging

Imaging was primarily performed on an Olympus FV3000RS confocal microscope (Olympus) using FLUOVIEW acquisition software (Olympus). General culture activity was acquired using a 60 $\times$  objective (Olympus; UPlanSApo 60 $\times$ /1.30 Sil) that contained  $\sim 200$  cells per field of view under normal plating conditions. Videos were acquired using a resonance scanner. RGE01 was detected using RFP filter settings (530 to 550 excitation/575 to 625 emission) with transmitted light channel acquired through a DIC prism. A 546-light-emitting diode laser level was set between 2 and 3.5%, pinhole aperture was opened to balance speed, and voltage was adjusted under a hi-lo lookup table to a level below saturation in all visible cells. Stacks were set to a range just below and just above the cells and optimized based on aperture size. The same acquisition settings were used for all samples in an imaging session as well as sampled compared between sessions. Flagellar beating videos were acquired as a single optical section using a 100 $\times$  objective (Olympus; UPlanSApo 100 $\times$ /1.40 Oil) with the pinhole fully opened using the resonance scanning setting. Perfusions were performed by manually pipetting (at times supported by a stabilizing stand and micromanipulator) a concentrated solution into the solution outside the microwell to minimize changes in flow over the cells and allow time for diffusion to occur before interacting with them.

### Image analysis

When stacks were acquired, summed projections were generated in FIJI (55) and RGE01 and DIC channels were separated. Primary analysis was performed using either FluoroSNNAPP (56) or Mesmerize (57) analysis platforms (fig. S16) as well as PeakCaller (58) for visualization of cell traces and basic features. In FluoroSNNAPP, image series were checked for motion artifacts and aligned if needed. Segmentation was performed using active contour over time-averaged series. Segmentation files were manually checked against DIC images and regions of interest (ROIs) were removed if needed. For high frame rate series (ciliary beating), ROIs were manually drawn for cells chosen based on the orientation of the beating plane. Baseline fluorescence was set to a 10-s window and 50th percentile. Functional connectivity was calculated with cross-correlation ( $N$  resampling 100, max time lag 0.5 s), partial correlation ( $\alpha$ -level significance 0.001), instantaneous phase ( $N$  resampling 100,  $\alpha$ -level significance 0.001), Granger causality (max model order 20,  $\alpha$ -level significance 0.05, with no. of iteration automatically detected), and transfer entropy ( $N$  resampling 100, lags 1:10). For Mesmerize (57) analysis, motion correction was performed using CaImAN (59) and NoRMCorre

(60), and ROIs were detected with CNMF(E) (61). Samples were then normalized and  $\Delta F/F_0$  was extracted and  $z$  scored. A Butterworth filter was used for smoothing. Automated peak detection was performed and then manually checked for artifacts. Peak features were then extracted. k-Shape clustering (62) was performed on  $\Delta F/F_0$  peak curves with the data divided into partitions between 4 and 8, created by sorting the peak curves according to peak width, with 100 different centroid seeds for each partition. A total of 100 iterations of the k-Shape clustering algorithm were performed with a tolerance of  $1 \times 10^{-6}$  and training was performed on 30% of the data (fig. S17). Data were input from 10 replicate cultures, over three independent experiments. For PeakCaller (58) visualization, extracted fluorescence from established ROIs was loaded. Parameters used were required rise, 60%; max lookback pts., 25; required fall, 60%; max lookahead pts., 25; over absolute %; trend control, finite difference diffusion (two sided); and trend smoothness, 60.

DIC images were analyzed in FIJI (55). For ciliary beating analysis, stacks were opened in LabKit plug-in (63) and manually annotated. Annotations were then opened in ImageJ and converted to binary masks. Masked files were converted to hyperstacks and temporal projections were generated over the full stack or on substacks within it.

### Functional imaging

CFM was prepared by excluding  $\text{Ca}^{2+}$  from ASW and including 10 mM EDTA. During plating, cells were washed into and maintained in CFM. To transfer cells to normal media, the upper volume of CFM was removed from the dish and replaced with high- $\text{Ca}^{2+}$  media (10 mM) and this was repeated with normal ASW. For gadolinium treatment, plated cells were mixed 1:1 with ASW containing 10  $\mu\text{M}$   $\text{Gd}^{3+}$  and then the dish was filled with ASW + 5  $\mu\text{M}$   $\text{Gd}^{3+}$ . For verapamil treatments, 2 $\times$  verapamil solution in ASW was added to plated cells after 20 min and they were incubated for an additional 10 min before imaging. For ionomycin treatments, stock solution (10 mg/ml in DMSO) was diluted to 2 $\times$  concentration in ASW and mixed 1:1 with cells. For perfusion assays, a 10 $\times$  ionomycin stock was gently pipetted in for a final 1 $\times$  concentration. For electric field stimulation, a stimulation chamber was fabricated in a glass-bottom dish. Wire channels were cut using a rotary saw and perpendicular platinum wires were fed through ~1 mm apart and affixed with silicone tape. A coverslip was fixed over the middle and cells were plated beneath this, between the electrodes. All wires were stabilized by rigid supports on the microscope table and pulses were delivered manually with an isolated stimulator (npi—ISO-STIM\_01D). For bacterial abundance assays, 40 ml of culture was collected and pelleted at 1500g for 5 min at room temperature, and the supernatant was discarded. The cells were then resuspended in 50 ml of ASW and shaken thoroughly before pelleting again. This was repeated 3 $\times$ . The washed pellet was then resuspended in 400  $\mu\text{l}$  of ASW and an aliquot was taken to check cell density. The cells were then diluted to better match previous experiments and plated. To replace washed bacteria, a 10-mg pellet of *E. pacifica* bacteria was resuspended in 500  $\mu\text{l}$  of ASW. For “low bacteria,” the cells were supplemented with 100  $\mu\text{l}$  of ASW, and for “high bacteria,” the cells were supplemented with 100  $\mu\text{l}$  of ASW containing 2  $\mu\text{g}$  of *E. pacifica*. Intermediate bacterial concentrations were obtained by diluting stock (20  $\mu\text{g}/\text{ml}$ ) in ASW.

### Supplementary Materials

#### The PDF file includes:

Figs. S1 to S17

Legends for movies S1 to S6

#### Other Supplementary Material for this manuscript includes the following:

Movies S1 to S6

### REFERENCES AND NOTES

1. X. Cai, X. Wang, S. Patel, D. E. Clapham, Insights into the early evolution of animal calcium signaling machinery: A unicellular point of view. *Cell Calcium* **57**, 166–173 (2015).
2. J. Colgren, P. Burkhardt, The premetazoan ancestry of the synaptic toolkit and appearance of first neurons. *Essays Biochem.* **66**, 781–795 (2022).
3. N. Ros-Rcoher, A. Pérez-Posada, M. M. Leger, I. Ruiz-Trillo, The origin of animals: An ancestral reconstruction of the unicellular-to-multicellular transition. *Open Biol.* **11**, 200359 (2021).
4. T. Brunet, N. King, The origin of animal multicellularity and cell differentiation. *Dev. Cell* **43**, 124–140 (2017).
5. J. Colgren, S. A. Nichols, MRTF specifies a muscle-like contractile module in Porifera. *Nat. Commun.* **13**, 4134 (2022).
6. P. Burkhardt, J. Colgren, A. Medhus, L. Digel, B. Naumann, J. J. Soto-Angel, E.-L. Nordmann, M. Y. Sachkova, M. Kittelmann, Syncytial nerve net in a ctenophore adds insights on the evolution of nervous systems. *Science* **380**, 293–297 (2023).
7. S. R. Najle, X. Grau-Bové, A. Elek, C. Navarrete, D. Cianferoni, C. Chiva, D. Cañas-Armenteros, A. Mallabiarrena, K. Kamm, E. Sabidó, H. Gruber-Vodicka, B. Schierwater, L. Serrano, A. Sebé-Pedrós, Stepwise emergence of the neuronal gene expression program in early animal evolution. *Cell* **186**, 4676–4693.e29 (2023).
8. A. Sebé-Pedrós, E. Chomsky, K. Pang, D. Lara-Astiaso, F. Gaiti, Z. Mukamel, I. Amit, A. Hejnal, B. M. Degnan, A. Tanay, Early metazoan cell type diversity and the evolution of multicellular gene regulation. *Nat. Ecol. Evol.* **2**, 1176–1188 (2018).
9. J. M. Musser, K. J. Schippers, M. Nickel, G. Mizzon, A. B. Kohn, C. Pape, P. Ronchi, N. Papadopoulos, A. J. Tarashansky, J. U. Hammel, F. Wolf, C. Liang, A. Hernández-Plaza, C. P. Cantalapiedra, K. Achim, N. L. Schieber, L. Pan, F. Ruperti, W. R. Francis, S. Vargas, S. Kling, M. Renkert, M. Polikarpov, G. Bourenkov, R. Feuda, I. Gaspar, P. Burkhardt, B. Wang, P. Bork, M. Beck, T. R. Schneider, A. Kreshuk, G. Wörheide, J. Huerta-Cepas, Y. Schwab, L. L. Moroz, D. Arendt, Profiling cellular diversity in sponges informs animal cell type and nervous system evolution. *Science* **374**, 717–723 (2021).
10. D. Arendt, The evolution of cell types in animals: Emerging principles from molecular studies. *Nat. Rev. Genet.* **9**, 868–882 (2008).
11. T. Brunet, D. Arendt, From damage response to action potentials: Early evolution of neural and contractile modules in stem eukaryotes. *Philos. Trans. R. Soc. Lond. B Biol. Sci.* **371**, 20150043 (2016).
12. X. Cai, Unicellular  $\text{Ca}^{2+}$  signaling “toolkit” at the origin of metazoa. *Mol. Biol. Evol.* **25**, 1357–1361 (2008).
13. D. Arendt, The evolutionary assembly of neuronal machinery. *Curr. Biol.* **30**, R603–R616 (2020).
14. M. Brini, T. Cali, D. Ottoloni, E. Carafoli, Intracellular calcium homeostasis and signaling. *Met. Ions Life Sci.* **12**, 119–168 (2013).
15. I. V. Shemarova, V. P. Nesterov, Evolution of mechanisms of  $\text{Ca}^{2+}$ -signaling. Role of  $\text{Ca}^{2+}$  in regulation of fundamental cell functions. *Zh. Evol. Biokhim. Fiziol.* **44**, 341–351 (2008).
16. S. L. A. Wang, Calcium signaling mechanisms across kingdoms. *Annu. Rev. Cell Dev. Biol.* **37**, 311–340 (2021).
17. M. J. Berridge, M. D. Bootman, H. L. Roderick, Calcium signalling: Dynamics, homeostasis and remodelling. *Nat. Rev. Mol. Cell Biol.* **4**, 517–529 (2003).
18. M. Brini, T. Cali, D. Ottoloni, E. Carafoli, Neuronal calcium signaling: Function and dysfunction. *Cell. Mol. Life Sci.* **71**, 2787–2814 (2014).
19. M. J. Berridge, Neuronal calcium signaling. *Neuron* **21**, 13–26 (1998).
20. H. Harz, P. Hegemann, Rhodopsin-regulated calcium currents in *Chlamydomonas*. *Nature* **351**, 489–491 (1991).
21. S. Lodh, J. Yano, M. S. Valentine, J. L. Van Houten, Voltage-gated calcium channels of Paramecium cilia. *J. Exp. Biol.* **219**, 3028–3038 (2016).
22. R. Docampo, S. N. Moreno, Calcium signaling in intracellular protist parasites. *Curr. Opin. Microbiol.* **64**, 33–40 (2021).
23. T. Hagihara, H. Mano, T. Miura, M. Hasebe, M. Toyota, Calcium-mediated rapid movements defend against herbivorous insects in *Mimosa pudica*. *Nat. Commun.* **13**, 6412 (2022).
24. Y. Moran, H. H. Zakon, The evolution of the four subunits of voltage-gated calcium channels: Ancient roots, increasing complexity, and multiple losses. *Genome Biol. Evol.* **6**, 2210–2217 (2014).

25. N. Ros-Rocher, T. Brunet, What is it like to be a choanoflagellate? Sensation, processing and behavior in the closest unicellular relatives of animals. *Anim. Cogn.* **26**, 1767–1782 (2023).
26. M. Carr, B. S. C. Leadbeater, R. Hassan, M. Nelson, S. L. Baldauf, Molecular phylogeny of choanoflagellates, the sister group to Metazoa. *Proc. Natl. Acad. Sci. U.S.A.* **105**, 16641–16646 (2008).
27. M. J. Dayel, R. A. Alegado, S. R. Fairclough, T. C. Levin, S. A. Nichols, K. McDonald, N. King, Cell differentiation and morphogenesis in the colony-forming choanoflagellate *Salpingoeca rosetta*. *Dev. Biol.* **357**, 73–82 (2011).
28. T. Brunet, M. Albert, W. Roman, M. C. Coyle, D. C. Spitzer, N. King, A flagellate-to-amoeboid switch in the closest living relatives of animals. *eLife* **10**, e61037 (2021).
29. D. Laundon, B. T. Larson, K. McDonald, N. King, P. Burkhardt, The architecture of cell differentiation in choanoflagellates and sponge choanocytes. *PLoS Biol.* **17**, e3000226 (2019).
30. R. A. Alegado, L. W. Brown, S. Cao, R. K. Dermenjian, R. Zuzow, S. R. Fairclough, J. Clardy, N. King, A bacterial sulfonolipid triggers multicellular development in the closest living relatives of animals. *eLife* **1**, e00013 (2012).
31. C. Nielsen, Six major steps in animal evolution: Are we derived sponge larvae? *Evol. Dev.* **10**, 241–257 (2008).
32. I. Ruiz-Trillo, A. de Mendoza, Towards understanding the origin of animal development. *Development* **147**, dev192575 (2020).
33. J. B. Kirkegaard, A. Bouillant, A. O. Marron, K. C. Leptos, R. E. Goldstein, Aerotaxis in the closest relatives of animals. *eLife* **5**, e18109 (2016).
34. G. L. Miño, M. A. R. Koehl, N. King, R. Stocker, Finding patches in a heterogeneous aquatic environment: pH-taxis by the dispersal stage of choanoflagellates. *Limnol. Oceanogr. Lett.* **2**, 37–46 (2017).
35. M. A. R. Koehl, Selective factors in the evolution of multicellularity in choanoflagellates. *J. Exp. Zool. B Mol. Dev. Evol.* **336**, 315–326 (2021).
36. W. E. Kumler, J. Jorge, P. M. Kim, N. Iftekhar, M. A. R. Koehl, Does formation of multicellular colonies by choanoflagellates affect their susceptibility to capture by passive protozoan predators? *J. Eukaryot. Microbiol.* **67**, 555–565 (2020).
37. M. B. Short, C. A. Solari, S. Ganguly, T. R. Powers, J. O. Kessler, R. E. Goldstein, Flows driven by flagella of multicellular organisms enhance long-range molecular transport. *Proc. Natl. Acad. Sci. U.S.A.* **103**, 8315–8319 (2006).
38. T. Cavalier-Smith, Origin of animal multicellularity: Precursors, causes, consequences-the choanoflagellate/sponge transition, neurogenesis and the Cambrian explosion. *Philos. Trans. R. Soc. Lond. B Biol. Sci.* **372**, 20150476 (2017).
39. T. Fenchel, Filter-feeding in colonial protists. *Protist* **170**, 283–286 (2019).
40. S. E. Kapsetaki, S. A. West, The costs and benefits of multicellular group formation in algae. *Evolution* **73**, 1296–1308 (2019).
41. S. P. Leys, The choanosome of hexactinellid sponges. *Invertebr. Biol.* **118**, 221 (1999).
42. S. P. Leys, Elements of a “nervous system” in sponges. *J. Exp. Biol.* **218**, 581–591 (2015).
43. S. P. Leys, G. O. Mackie, H. M. Reisinger, The biology of glass sponges. *Adv. Mar. Biol.* **52**, 1–145 (2007).
44. H. Nguyen, E. Ross, R. Cortez, L. Fauci, M. A. R. Koehl, Effects of prey capture on the swimming and feeding performance of choanoflagellates. *Flow* **3**, E22 (2023).
45. S. Sorensen, S. S. Asadzadeh, J. H. Walther, Hydrodynamics of prey capture and transportation in choanoflagellates. *Fluids* **6**, 94 (2021).
46. B. S. C. Leadbeater, *The Choanoflagellates* (Cambridge Univ. Press, 2014).
47. K. Y. Wan, G. Jékely, Origins of eukaryotic excitability. *Philos. Trans. R. Soc. Lond. B Biol. Sci.* **376**, 20190758 (2021).
48. K. Dunlap, Localization of calcium channels in *Paramecium caudatum*. *J. Physiol.* **271**, 119–133 (1977).
49. R. G. Endres, N. S. Wingreen, Accuracy of direct gradient sensing by single cells. *Proc. Natl. Acad. Sci. U.S.A.* **105**, 15749–15754 (2008).
50. R. G. Endres, N. S. Wingreen, Accuracy of direct gradient sensing by cell-surface receptors. *Prog. Biophys. Mol. Biol.* **100**, 33–39 (2009).
51. J. B. Kirkegaard, A. O. Marron, R. E. Goldstein, Motility of colonial choanoflagellates and the statistics of aggregate random walkers. *Phys. Rev. Lett.* **116**, 038102 (2016).
52. H. Laeverenz-Schlogelhofer, K. Y. Wan, Bioelectric control of locomotor gaits in the walking ciliate *Euplotes*. *Curr. Biol.* **34**, 697–709.e6 (2024).
53. D. S. Booth, H. Szmidt-Middleton, N. King, Transfection of choanoflagellates illuminates their cell biology and the ancestry of animal septins. *Mol. Biol. Cell* **29**, 3026–3038 (2018).
54. P. Puigbò, E. Guzmán, A. Romeu, S. García-Vallvé, OPTIMIZER: A web server for optimizing the codon usage of DNA sequences. *Nucleic Acids Res.* **35**, W126–31 (2007).
55. J. Schindelin, I. Arganda-Carreras, E. Frise, V. Kaynig, M. Longair, T. Pietzsch, S. Preibisch, C. Rueden, S. Saalfeld, B. Schmid, J.-Y. Tinevez, D. J. White, V. Hartenstein, K. Eliceiri, P. Tomancak, A. Cardona, Fiji: An open-source platform for biological-image analysis. *Nat. Methods* **9**, 676–682 (2012).
56. T. P. Patel, K. Man, B. L. Firestein, D. F. Meaney, Automated quantification of neuronal networks and single-cell calcium dynamics using calcium imaging. *J. Neurosci. Methods* **243**, 26–38 (2015).
57. K. Kolar, D. Dondorp, J. C. Zwigelaar, J. Høyer, M. Chatzigeorgiou, Mesmerize is a dynamically adaptable user-friendly analysis platform for 2D and 3D calcium imaging data. *Nat. Commun.* **12**, 6569 (2021).
58. E. Artimovich, R. K. Jackson, M. B. C. Kilander, Y.-C. Lin, M. W. Nestor, PeakCaller: An automated graphical interface for the quantification of intracellular calcium obtained by high-content screening. *BMC Neurosci.* **18**, 72 (2017).
59. A. Giovannucci, J. Friedrich, P. Gunn, J. Kalfon, B. L. Brown, S. A. Koay, J. Taxis, F. Najafi, J. L. Gauthier, P. Zhou, B. S. Khakh, D. W. Tank, D. B. Chklovskii, E. A. Pnevmatikakis, CalmAn: an open source tool for scalable calcium imaging data analysis. *eLife* **8**, e38173 (2019).
60. E. A. Pnevmatikakis, A. Giovannucci, NoRMCorr: An online algorithm for piecewise rigid motion correction of calcium imaging data. *J. Neurosci. Methods* **291**, 83–94 (2017).
61. L. M. Tran, A. J. Mocle, A. I. Ramsaran, A. D. Jacob, P. W. Frankland, S. A. Josselyn, Automated curation of CNMF-E-extracted ROI spatial footprints and calcium traces using open-source AutoML tools. *Front. Neural Circuits* **14**, 42 (2020).
62. C. Chira, J. Sedano, M. Camara, C. Prieto, J. R. Villar, E. Corchado, A cluster merging method for time series microarray with production values. *Int. J. Neural Syst.* **24**, 1450018 (2014).
63. M. Arzt, J. Deschamps, C. Schmied, T. Pietzsch, D. Schmidt, P. Tomancak, R. Haase, F. Jug, LABKIT: Labeling and segmentation toolkit for big image data. *Front. Comput. Sci.* **4**, 777728 (2022).

**Acknowledgments:** We thank all members of the Burkhardt group, past and present, for thoughtful discussions. We would also like to particularly thank A. Ravi and R. Göhde for assistance with the choanoflagellate cultures. We thank M. Chatzigeorgiou and T. Lynagh for conceptual and technical assistance with this work, and we thank S. Nichols for valuable feedback on the manuscript. **Funding:** This work was supported by the Michael Sars Centre core budget. **Author contributions:** J.C. and P.B. conceptualized and designed the research. J.C. generated the choanoflagellate line. J.C. collected and analyzed imaging data. J.C. and P.B. wrote the manuscript. **Competing interests:** The authors declare that they have no competing interests. **Data and materials availability:** All data have been deposited in FigShare (DOI:10.6084/m9.figshare.26065234). SRGECO1 expression plasmid is deposited at Addgene (ID 222940). All data needed to evaluate the conclusions in the paper are present in the paper and/or the Supplementary Materials.

Submitted 15 July 2024  
Accepted 4 December 2024  
Published 8 January 2025  
10.1126/sciadv.adr7434